



Synergizing lattice strain and electron transfer in TMSs@1 T-MoS₂ in-plane heterostructures for efficient hydrogen evolution reaction

Kaiwen Wang, Kaifeng Yu, Shaonan Xu, Shisheng Yuan, Lijuan Xiang, Bingxue Pang, Jiaqi Zheng, Nan Li^{*}

Key Laboratory of Automobile Materials (Ministry of Education), School of Materials Science and Engineering, Jilin University, 2699 Qianjin Street, Changchun 130012, PR China

ARTICLE INFO

Keywords:

1 T phase molybdenum disulfide
Electron effect
Hydrogen evolution reaction
In-plane heterostructure
Strain effect

ABSTRACT

The 1 T phase molybdenum disulfide (1 T-MoS₂) is considered a promising candidate to replace Pt-based catalysts for the hydrogen evolution reaction (HER). However, the less-active sites on the basal plane limit its electrocatalytic activity. Herein, we designed an in-plane heterostructure with transition metal sulfide (TMSs) clusters embedded in the 1 T-MoS₂ nanosheets by substituting a portion of MoS₂ nanodomains (TMSs@1 T-MoS₂). Experimental and DFT results suggest that this unique structure induces lattice distortion of 1 T-MoS₂ and electron transfer at the heterointerfaces from the TMSs to the 1 T-MoS₂. Both factors synergistically regulate the electronic structure of the basal plane, thus improving hydrogen adsorption. Consequently, the TMSs@1 T-MoS₂ exhibited significantly enhanced HER activity. In particular, NiS₂@1 T-MoS₂ delivered 10 mA cm⁻² at low overpotentials of 73 mV and 71 mV in 0.5 M H₂SO₄ and 1.0 M KOH, respectively.

1. Introduction

Molybdenum disulfide (MoS₂) is a two-dimensional layer material with in-plane Mo-S covalent bonds and out-of-plane van der Waals interactions [1–4]. The anisotropic structure endows it with considerable specific surface area, rapid charge transfer, and convenient diffusion paths for reactants and products [5,6]. Among the three typical polytypes of MoS₂, i.e., 2 H, 1 T, and 3 R, 1 T phase MoS₂ (1 T-MoS₂) has received substantial attention in the field of electrochemistry for its metal-like conductivity [7–10]. Additionally, 1 T-MoS₂ reveals electrocatalytic activity towards the hydrogen evolution reaction (HER) on both edges and basal planes, making it a promising HER catalyst [11, 12]. However, the basal planes where most atoms are located are less active than the edge sites [13,14]. Therefore, activating the basal plane is desirable for the achievement of highly efficient catalysts.

The catalytic activity of the basal plane is restricted by the presence of saturated coordinated sulfur atoms and the difficulty of their interaction with reactants. To activate the basal plane, various methods based on electron structural modulation [15,16], including anion/cation doping [17,18], vacancy engineering [19], heterostructure construction [20], etc., have been used to modify the electron structure of sulfur atoms. Among them, the construction of heterostructures is a

controllable and reproducible method [21]. The heterostructures based on 1 T-MoS₂ can be classified into two types in terms of the combination mode of the heterogeneous phases [22–24]. One is the edge-on-layer mode, where the 1 T-MoS₂ nanosheets are grown vertically on the surface of supports [25–27]. Obviously, the heterointerfaces are located at the edges of the nanosheets and the electrons of the basal sulfur atoms are barely disturbed. Another is the layer-on-layer mode, where the 1 T-MoS₂ nanosheets lie parallelly on the top of the support that has a similar layered structure [28–31]. The cohesive force that bonds the two phases together is normally van der Waals interactions or electrostatic force, resulting from the coordination saturation of basal plane atoms. Such a weak interaction makes it difficult to regulate the electronic structure. In addition, the heterogeneous phases are in different planes, which will block the heterointerfaces and reduce their accessibility to reactants. Moreover, in both modes, the loaded phases are prone to overgrow because of lacking spatial restriction, which will lead to a decline in the number of heterointerfaces.

Herein, we designed an in-plane heterostructure, where the second phase was embedded in the 1 T-MoS₂ nanosheets by substituting a portion of MoS₂ nanodomains. In this structure, the chemical bond that connects the heterogeneous phases brings about strong interaction, including electronic interaction and lattice distortion, which can

^{*} Corresponding author.

E-mail address: lin@jlu.edu.cn (N. Li).

<https://doi.org/10.1016/j.apcatb.2023.122445>

Received 27 November 2022; Received in revised form 17 January 2023; Accepted 8 February 2023

Available online 10 February 2023

0926-3373/© 2023 Elsevier B.V. All rights reserved.

effectively modulate the electronic structure of the sulfur atoms in the basal plane. Moreover, the heterogeneous phases are located at the same plane, which can avoid steric effects and provide a structural basis for full exposure of the catalytic active sites. Furthermore, the spatial effects can constrain the size of the second phase and generate a large number of heterointerfaces. In this work, we selected transition metal sulfides (TMSs) as the second phase because their variable electronic structure and abundant electrons in the d orbital are in favor of electron modulation [32,33]. TMSs and 1 T-MoS₂ can share bridging sulfur at the interface to get stable heterostructures. We developed a one-step hydrothermal method to prepare this unique in-plane heterostructure, where transition metal molybdates (TM(MO₄)_x, TM = Fe, Co, Ni), which are insoluble at room temperature, served as homologous precursors for molybdenum and transition metals. During the hydrothermal reaction, the precursor progressively dissolved and the transition metal and molybdenum were synchronously released into the solution. Subsequently, they were simultaneously sulfated and the TMSs were in situ embedded in the nanosheets of 1 T-MoS₂, generating TMSs@ 1 T-MoS₂ in-plane heterostructures. As expected, these in-plane heterostructural catalysts exhibited significantly improved catalytic activity for hydrogen evolution as compared to 1 T-MoS₂. In particular, NiS₂ @ 1 T-MoS₂ outperformed most 1 T-MoS₂-based catalysts, with small overpotentials of 73 and 71 mV to deliver 10 mA cm⁻² in acidic and alkaline solutions, respectively. Theoretical calculations revealed that the insertion of TMSs induces tensile stresses in the 1 T-MoS₂ lattice and injects electrons into the Mo atoms, which synergistically regulate the electronic structure, leading to an activated basal plane and excellent conductivity, thus resulting in high catalytic activity.

2. Experimental section

2.1. Synthesis of catalysts

Transition metal nitrate (TM(NO₃)_x·xH₂O, TM = Fe, Co, Ni) and sodium molybdate (Na₂MoO₄·2 H₂O) with a molar ratio of TM: Mo = 1:1 were dissolved in 50 ml of deionized water. The solution was severely stirred at room temperature (for Fe, Co) or hydrothermally treated at 150 °C for 6 h (for Ni) to get a precipitate. The precipitate was transferred to a tube furnace and annealed at 500 °C for 2 h under an Ar atmosphere to obtain precursor TM(MoO₄)_x.

Afterward, 0.5 mmol of the as-prepared TM(MoO₄)_x and 10 mmol thiourea (CS(NH₂)₂) were dispersed in 20 ml of deionized water. This mixture, together with a piece of carbon cloth (2 cm × 3 cm) cleaned previously with 3 M HCl, deionized water, and ethanol, was put in a 50 ml Teflon-lined stainless-steel autoclave and then hydrothermally treated at 200 °C for 24 h. After cooling to room temperature, the carbon cloth was rinsed thoroughly with deionized water and ethanol several times to get carbon cloth-supporting TMSs@ 1 T-MoS₂.

The control sample 1 T-MoS₂ nanosheets (NSs) was synthesized by the same method as TMSs@ 1 T-MoS₂, except that TM(MoO₄)_x was replaced by Na₂MoO₄·2 H₂O. The Pt/C electrode was used as the benchmark catalyst which was prepared by first ultrasonicing commercial Pt/C powder with 1 ml ethanol and 50 μl Nifion and then dropping on the carbon cloth. The mass loading of Pt/C powder was consistent with TMSs@ 1 T-MoS₂.

2.2. Material characterization

The microstructure and morphology of samples were examined by scanning electron microscopy (SEM, JEOL JSM-6700 F) and transmission electron microscopy (TEM, JEOL JEM-2100 F). The TEM samples were prepared by peeling off TMSs@ 1 T-MoS₂ nanosheets from carbon cloth through ultrasonic treatment. TEM coupled with energy-dispersive X-ray spectroscopy (TEM-EDS) analyses were conducted to analyze the element constitution. X-ray diffraction (XRD) tests were performed using a DX2700 diffractometer with a Cu Kα radiation source

(λ = 0.15406 nm) in the 2θ range of 5–80°. Raman spectra were collected from a micro-Raman spectrometer (Renishaw) with a laser of 532 nm wavelength. X-ray photoelectron spectra (XPS) were recorded on an ESCALAB 250 electron spectrometer with an Al Kα radiation source (hν = 1486.6 eV). The mass loading of active materials on the carbon cloth is 0.6–0.7 mg cm⁻², based on the results of inductively coupled plasma atomic emission spectroscopy (ICP-AES, HORIBA) analysis.

2.3. Electrochemical measurement

Electrochemical tests were carried out on a Princeton Applied Research Parstat 3000-DX with a three-electrode system in N₂-saturated 0.5 M H₂SO₄ and 1.0 M KOH. The self-supporting TMSs@ 1 T-MoS₂ or other control samples directly served as the working electrode. A graphite rod and a saturated calomel electrode served as the counter electrode and reference electrode, respectively. All potentials were referenced to the reversible hydrogen electrode (RHE). Linear sweep voltammetry (LSV) measurements were scanned from 0 to −0.4 V vs. RHE at a rate of 2 mV·s⁻¹ with iR correction. Tafel slopes were derived from the corresponding LSV data by fitting into the equation: η = a + b·log j (η and j represent potential and current density, respectively; a and b are constants, and b is the Tafel slope). Chronoamperometry curves were recorded under a static overpotential of −0.1 V vs. RHE to estimate the electrochemical stability in 0.5 M H₂SO₄ or 1.0 M KOH. Electrochemical impedance spectra (EIS) were recorded within frequencies ranging from 10 kHz to 0.01 Hz at a potential of −0.2 V vs. RHE in 0.5 M H₂SO₄ or −0.3 V vs. RHE in 1.0 M KOH, and the impedance data were fitted to a simple Randles circuit to get charge transfer resistance. The exchange current density (j₀) was calculated by extrapolating the Tafel plot. Cyclic voltammetry (CV) measurements were conducted from 0.05 to −0.05 V vs. RHE at a suite of scan rates in the range of 20–100 mV·s⁻¹ with a 20 mV·s⁻¹ interval to evaluate electrochemical double-layer capacity (C_{edl}). Specifically, the C_{edl} is estimated by plotting the (ΔJ = J_a − J_c) as a function of the scan rate. The differences in ΔJ plotted against the scan rates were fitted to linear regression and the slope is twice the C_{edl}. The calculation details of turnover frequency (TOF) are shown in [Supporting Information](#).

2.4. DFT calculation

All DFT calculations were performed using Vienna Ab initio Simulation Package (VASP) [34]. The projector augmented wave (PAW) pseudopotential [35] with the PBE generalized gradient approximation (GGA) exchange-correlation function [36] was utilized in the computations. The cutoff energy of the plane waves basis set was 500 eV and a Monkhorst-Pack mesh of 3 × 3 × 1 was used in K-sampling in the adsorption energy calculation. The empirical correction in Grimme's method (DFT-D3) was employed to treat the van der Waals interactions. All atoms were fully relaxed with the energy convergence tolerance of 10⁻⁵ eV per atom, and the final force on each atom was < 0.01 eV Å⁻¹. All periodic slabs had a vacuum layer of at least 15 Å. All the atoms could relax.

The adsorption energy of reaction intermediates can be computed using the following Eqs. (1)–(2):

$$\Delta E_H = E_{*H} - (E_* + E_H) \quad (1)$$

$$\Delta G_H = \Delta E_H + \Delta E_{ZPE} - T\Delta S \quad (2)$$

Where ΔE_{ZPE} is the zero-point energy change, ΔS is the entropy change. In this work, the values of ΔE_{ZPE} and ΔS were obtained by vibration frequency calculation [37].

The formation energy of 1 T-MoS₂ and other models are calculated as Eq. (3):

$$\Delta E_f = (E_{Mox}S_yM_z - xE_{Mo} - yE_S - zE_M) / (x + z) \quad (M = Co, Fe, Ni) \quad (3)$$

Where E_{Mo} , E_{S} , and E_{M} are calculated from bulk material, and x , y , and z are the atomic number of the corresponding element in the material.

3. Results and discussion

3.1. Structure characterization of TMSs@ 1 T-MoS₂

The preparation process of the TMSs@ 1 T-MoS₂ in-plane heterostructure is illustrated in Fig. 1. First, transition metal molybdate (TM (MoO₄)_x, TM = Fe, Co, Ni), which is insoluble at room temperature, was precipitated from the solution and served as a homologous precursor for TM and Mo. The purity of the TM(MoO₄)_x precursors was validated by X-ray diffraction (XRD) (Fig. S1). Then, the TM(MoO₄)_x was converted to sulfide through a hydrothermal reaction. During this process, the precursor progressively dissolved and the transition metal and molybdenum were synchronously released into the solution. Subsequently, they were simultaneously sulfured due to the excess sulfur source, whereby TMSs were in situ embedded in the nanosheets of 1 T-MoS₂ to generate TMSs@ 1 T-MoS₂ in-plane heterostructure. By adding carbon cloth to the hydrothermal autoclave, the TMSs@ 1 T-MoS₂ nanosheets were grown on carbon cloth to get a self-supporting electrode. The morphology and microstructure of the samples were observed by scanning electron microscopy (SEM) and transmission electron microscopy (TEM). SEM images (Fig. S2) show that the TMSs@ 1 T-MoS₂ nanosheets are grown vertically on carbon cloth fibers, which is identical to the control sample 1 T-MoS₂ NSs. TEM images (Fig. 2a-d) indicate that each TMSs@ 1 T-MoS₂ nanosheet has a multilayer structure with interlayer spacings of 6.81 Å (FeS₂ @ 1 T-MoS₂), 6.72 Å (CoS₂ @ 1 T-MoS₂) and 6.75 Å (NiS₂ @ 1 T-MoS₂), respectively, which are much smaller than the 1 T-MoS₂ NSs (9.16 Å). It suggests that the incorporation of TMSs leads to a shrinkage of layers. High-resolution (HR)TEM images (Fig. 2e-h) show clearly the trigonal atomic arrangement of 1 T-MoS₂ and orthorhombic (FeS₂) or cubic (CoS₂, NiS₂) atomic arrangements of TMSs, which are consistent with their standard structural configurations (insertion in Fig. 2e-h). In addition, well-defined grain boundaries are observed between the different phases, suggesting that TMSs are implanted in the 1 T-MoS₂ nanosheet rather than loaded on its top. Moreover, the nanosheet containing both TMSs and MoS₂ domains display consistent contrast under the electron beam, which reveals their comparable atomic thicknesses and further confirms the successful construction of in-plane heterostructure. The size of TMSs crystal domains is as small as ~5 nm owing to the spatial confinement of the embedded structure. The lattice spacings of 2.68, 2.77, 2.76, and 2.85 Å correspond to the (101) and (020) crystal planes of orthorhombic FeS₂, (200) crystal plane of cubic CoS₂, and (200) crystal plane of cubic NiS₂, respectively. Furthermore, compared to the (100) lattice spacing of 2.72 Å in 1 T-MoS₂ NSs, the corresponding spacing of TMSs@ 1 T-MoS₂ expands to 2.78 (FeS₂ @ 1 T-MoS₂), 2.81 (CoS₂ @ 1 T-MoS₂) and 2.82 Å (NiS₂ @ 1 T-MoS₂), suggesting the incorporation of TMSs induces transverse tensile stress into 1 T-MoS₂ lattice. Geometric phase analysis (GPA) further confirmed the tensile stress (Fig. 2i-l and S3). The strain tensor (ϵ_{xx} , ϵ_{xy} and ϵ_{yy}) on the TMSs@ 1 T-MoS₂ basal plane reveals a

tensile condition, suggesting that the implanting of TMSs exerts 1 T-MoS₂ in tension. This is in contrast to the basal plane of 1 T-MoS₂ NSs, which is subject to almost stress-free or slight compressive stresses. Energy dispersive X-ray spectroscopy (EDX) analysis verifies the uniform distribution of Mo, S, and Fe/Co/Ni elements in the samples (Fig. S4), suggesting that TMSs' crystalline domains are small and disperse evenly in the nanosheets. The content of elements was detected by inductively coupled plasma atomic emission spectroscopy (ICP-AES) (detailed data in Table S1). The molar ratio of (TM + Mo):S is about 1:2, which is consistent with the stoichiometric ratio. The molar ratio of TM:Mo is approximately 1:2.5, revealing a high TM content and hence a massive content of heterointerfaces.

The crystallographic structures of TMSs@ 1 T-MoS₂ were examined by XRD (Fig. S5). In addition to the 24° peak arising from carbon cloth, all samples display characteristic diffractions of MoS₂. By comparing TMSs@ 1 T-MoS₂ and 1 T-MoS₂ NSs, it is evident that the (002) peaks of TMSs@ 1 T-MoS₂ shift to larger angles while the (100) peaks shift slightly to smaller angles. It agrees with the TEM images that TMSs@ 1 T-MoS₂ nanosheets have enlarged (100) interplanar spacing and contracted interlayer spacing. In addition, compared to the strong and sharp (002) peak of 1 T-MoS₂ NSs which only exhibits a full width at half maximum (FWHM) of 0.49°, the (002) peaks of TMSs@ 1 T-MoS₂ samples are notably less intense and broader, with larger FWHM of 0.67°, 0.67° and 0.72° for FeS₂ @ 1 T-MoS₂, CoS₂ @ 1 T-MoS₂, and NiS₂ @ 1 T-MoS₂, respectively. It suggests that the stacking of layers is less ordered. However, no obvious diffractions from TMSs were detected in the XRD patterns, signifying the TMSs grains are tiny and lack long-range ordering, as consistent with the HRTEM observation.

The presence of the 1 T phase in the heterostructure was verified by Raman spectra (Fig. S6). The peaks at 145, 238, and 335 cm⁻¹ are attributed to characteristic vibrational modes of J₁, J₂, and J₃ from 1 T phase MoS₂, while the peaks at 280, 373, and 402 cm⁻¹ are assigned as vibrational modes of E_g¹, E_g² and A_{1g} of 2 H phase. The above results suggest the samples consist of 1 T/2 H mixed phases. Additionally, the blueshift of the E_g² and A_{1g} vibrations in comparison to the 1 T-MoS₂ NSs suggests that the TMSs@ 1 T-MoS₂ are less ordered.

We analyzed the surface chemical composition and valence state of TMSs@ 1 T-MoS₂ using X-ray photoelectron spectroscopy (XPS). The Mo 3d spectrum of 1 T-MoS₂ NSs is deconvoluted into two doublets (Fig. S7a), which are attributed to Mo⁴⁺ in 1 T-MoS₂ [228.9 eV (Mo 3d_{5/2}) and 232.2 eV (Mo 3d_{3/2})], and Mo⁴⁺ in 2 H-MoS₂ [229.8 eV (Mo 3d_{5/2}) and 233.1 eV (Mo 3d_{3/2})]. It confirms the coexistence of 1 T and 2 H phase MoS₂. Based on the peak area, the 1 T phase accounts for 69.4%. The Mo⁴⁺ (1 T) peaks in FeS₂ @ 1 T-MoS₂, CoS₂ @ 1 T-MoS₂, and NiS₂ @ 1 T-MoS₂ shift 0.1, 0.1 and 0.3 eV, respectively, toward the lower binding energy relative to 1 T-MoS₂ NSs. It is an indication that the electron density on Mo increases, which is attributed to the electron transfer from TMSs to MoS₂. The content of 1 T phase in FeS₂ @ 1 T-MoS₂, CoS₂ @ 1 T-MoS₂, and NiS₂ @ 1 T-MoS₂ are 79.8%, 79.3%, and 74.4%, respectively, which are higher than that in 1 T-MoS₂ NSs. It suggests that the increase in electron density of Mo improves the stability of 1 T phase MoS₂. The S 2p spectra of TMSs@ 1 T-MoS₂ (Fig. S7b)

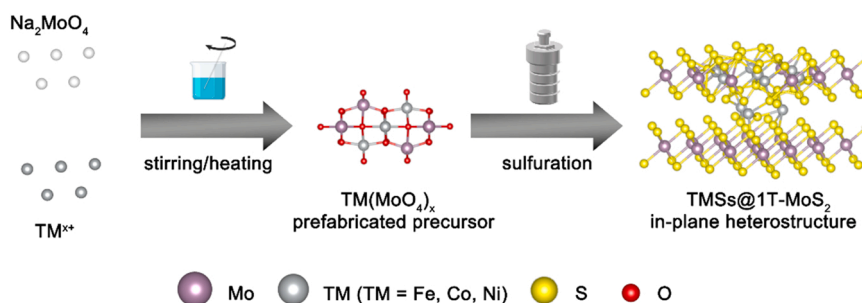


Fig. 1. Schematic illustration of the synthesis process of TMSs@ 1 T-MoS₂.

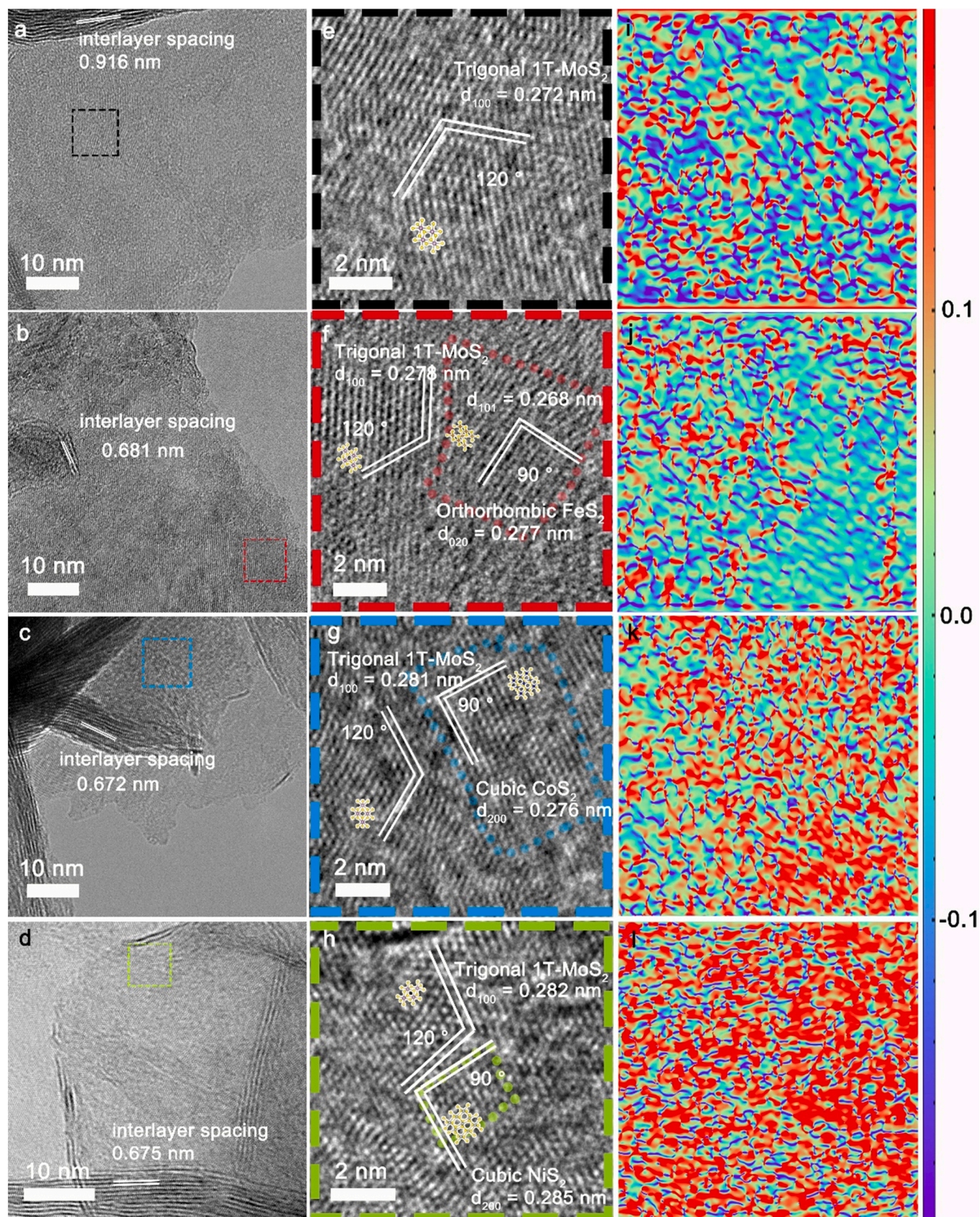


Fig. 2. (a-d) TEM, (e-h) HRTEM images of 1 T-MoS₂ NSs and TMSs@ 1 T-MoS₂, and (i-l) ϵ_{yy} strain component determined via GPA of TMSs@ 1 T-MoS₂. The inserts in (e-h) are structural configurations of 1 T-MoS₂ and TMSs. (a,e) 1 T-MoS₂ NSs, (b,f) FeS₂ @ 1 T-MoS₂, (c,g) CoS₂ @ 1 T-MoS₂, and (d,h) NiS₂ @ 1 T-MoS₂.

are deconvoluted into three doublets, including S^{2-} [163.1 (S 2p_{1/2}) and 161.8 eV (S 2p_{3/2})] in MoS₂, S^{2-} [164.6 (S 2p_{1/2}) and 162.5 eV (S 2p_{3/2})] in TMSs, and bridging S between MoS₂ and TMSs [163.6 (S 2p_{1/2}) and 162.3 eV (S 2p_{3/2})]. The negative shift of S^{2-} peaks in TMSs@1 T-MoS₂ relative to 1 T-MoS₂ NSs (0.3, 0.4, and 0.2 eV for FeS₂@1 T-MoS₂, CoS₂@1 T-MoS₂, and NiS₂@1 T-MoS₂) implies an increase in the electron density of S resulting from the electron accumulation on MoS₂. In addition, the appearance of bridging S indicates that TMSs and 1 T-MoS₂ are covalently connected via S. In the Fe 2p spectrum of FeS₂@1 T-MoS₂ (Fig. S7c), in addition to the doublet of Fe²⁺ [721.2 (Fe 2p_{1/2}) and 708.3 eV (Fe 2p_{3/2})], a weak doublet of Fe³⁺ [723.4 (Fe 2p_{1/2}) and 710.5 eV (Fe 2p_{3/2})] is also detected, as a result of partial surface oxidation. The Co 2p spectrum in CoS₂@1 T-MoS₂ (Fig. S7d) exhibits two doublets. The existence of CoS₂ is identified by the doublet at 794.6 eV (Co 2p_{1/2}) and 779.7 eV (Co 2p_{3/2}) that are attributable to Co²⁺, along with two satellite peaks. Similarly, the Ni 2p spectrum of NiS₂@1 T-MoS₂ (Fig. S7e) shows two doublets, including a doublet of Ni²⁺ [861.1 (Ni 2p_{1/2}) and 854.9 eV (Ni 2p_{3/2})] and a satellite doublet.

4. Electrochemical Performance of TMSs@1 T-MoS₂

The TMSs@1 T-MoS₂ and 1 T-MoS₂ NSs catalysts supported on carbon were directly used as self-supporting electrodes for the hydrogen evolution reaction in acidic and alkaline electrolytes. First, the catalytic performance was evaluated in N₂-saturated 0.5 M H₂SO₄ by linear scanning voltammetry (LSV), and the results were compared with 1 T-MoS₂ NSs and 20 wt% Pt/C (Fig. 3a). The order of catalytic activity follows 1 T-MoS₂ NSs < FeS₂@1 T-MoS₂ < CoS₂@1 T-MoS₂ < NiS₂@1 T-MoS₂. Specifically, the 1 T-MoS₂ NSs require a larger overpotential of 184 mV to achieve a current density of 10 mA cm⁻² (η_{10}), as consistent with previous reports [49,50]. All TMSs@1 T-MoS₂ catalysts display markedly increased activity with η_{10} decreasing to 96, 80, and 73 mV for FeS₂@1 T-MoS₂, CoS₂@1 T-MoS₂, and NiS₂@1 T-MoS₂,

respectively. Additionally, all TMSs@1 T-MoS₂ catalysts exhibit lower Tafel slopes than 1 T-MoS₂ NSs (115 mV dec⁻¹) (Fig. 3b), which are 75, 69, and 67 mV dec⁻¹ for FeS₂@1 T-MoS₂, CoS₂@1 T-MoS₂, and NiS₂@1 T-MoS₂, respectively, suggesting the kinetics are dramatically accelerated. Especially, NiS₂@1 T-MoS₂ outperforms most 1 T-MoS₂-based catalysts (Table S2 and Fig. 3c) in terms of η_{10} and Tafel slope. The electrochemical stability of TMSs@1 T-MoS₂ in 0.5 M H₂SO₄ was evaluated via 30 h chronoamperometry (Fig. 3d). In contrast to the 1 T-MoS₂ NSs that only maintains 66% of the initial current density, all TMSs@1 T-MoS₂ catalysts maintain more than 93% of the current density, indicating their excellent electrochemical stability. SEM observation (Fig. S8) and XPS results (Fig. S9) on the post-chronoamperometry catalyst show similar morphology and surface composition as the original catalysts, further confirming the structural stability. Moreover, the electrochemical impedance spectra (EIS) reveal (Fig. S10) that the charge transfer resistances (R_{ct}) of CoS₂@1 T-MoS₂ (4.0 Ω) and NiS₂@1 T-MoS₂ (6.3 Ω) are much reduced as compared to 1 T-MoS₂ NSs (44.7 Ω), allowing rapid electron transfer between the electrode and the electrolyte. Furthermore, TMSs@1 T-MoS₂ catalysts exhibit higher exchange current densities (j_0) than 1 T-MoS₂ NSs, as illustrated in Fig. 3e. In particular, NiS₂@1 T-MoS₂ exhibits the highest j_0 (809 μ A cm⁻²) among the catalysts, which is 3.2 times larger than that of 1 T-MoS₂ NSs (249 μ A cm⁻²) and is comparable to the benchmark Pt/C (834 μ A cm⁻²).

To evaluate the intrinsic activity, we normalized the LSV curves with the electrochemical surface area (ECSA) obtained from the electrochemical double-layer capacity (C_{dl}) to exclude the influence of the number of active sites (Fig. S11). At -0.2 V, FeS₂@1 T-MoS₂, CoS₂@1 T-MoS₂ and NiS₂@1 T-MoS₂ reach current densities of -0.60, -0.74 and -0.97 mA mF⁻¹, respectively, which are much higher than 1 T-MoS₂ NSs (-0.11 mA mF⁻¹). Besides, we calculated the turnover frequency (TOF) based on the exchange current density (j_0) and ECSA (Fig. 3f). The TOF values of FeS₂@1 T-MoS₂, CoS₂@1 T-MoS₂, and

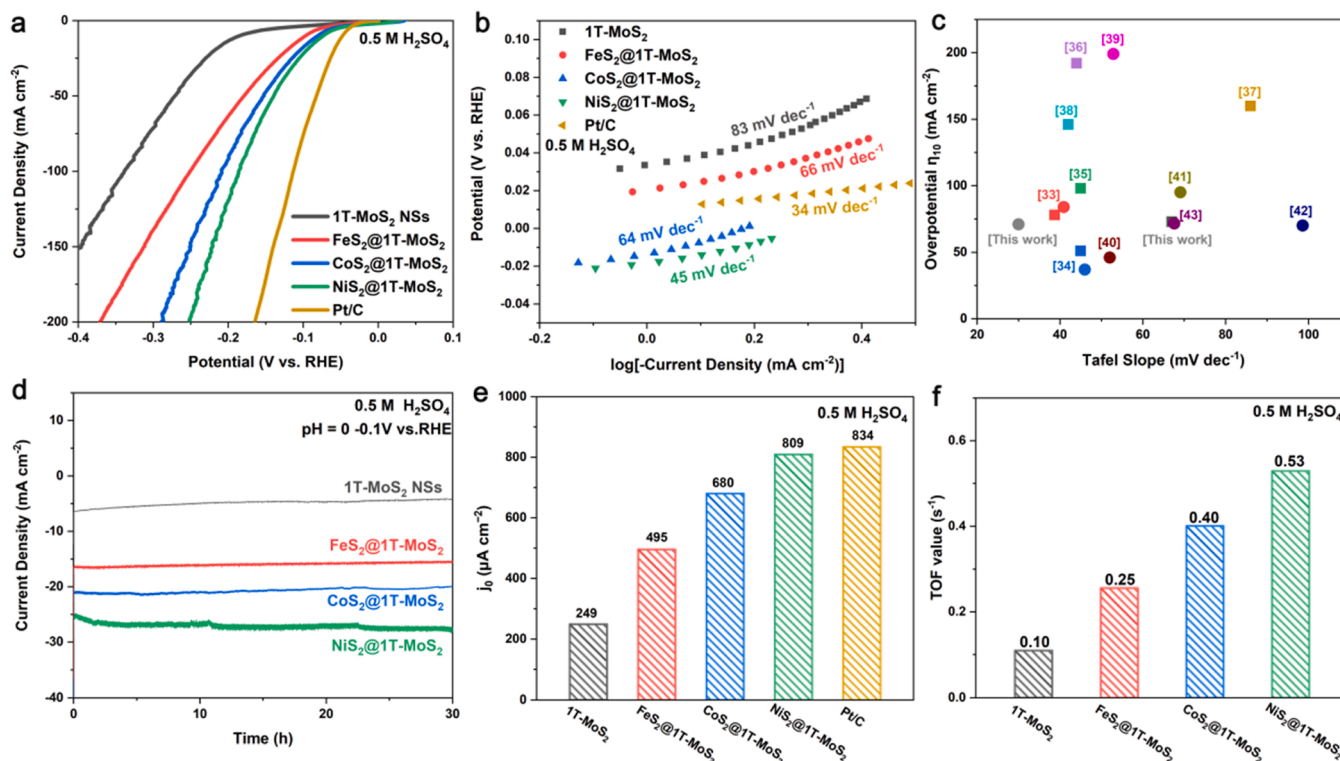


Fig. 3. Electrochemical performance of TMSs@1 T-MoS₂ in 0.5 M H₂SO₄. a) LSV curves and b) corresponding Tafel slopes of 1 T-MoS₂ NSs and TMSs@1 T-MoS₂. c) An activity comparison of recently reported 1 T-MoS₂-based catalysts and NiS₂@1 T-MoS₂ in this work (■: acidic, ●: alkaline) [38–48]. d) chronoamperometry curves, e) exchange current densities (j_0), and f) turnover frequencies (TOF) values of 1 T-MoS₂ NSs and TMSs@1 T-MoS₂.

NiS₂ @ 1 T-MoS₂ are 0.25, 0.40, and 0.53 s⁻¹, respectively, which are 2.5, 4, and 5 times higher than the 1 T-MoS₂ NSs (0.10 s⁻¹). Considering that the actual sulfur sites are limited to the heterointerfaces, whereas the TOF values are calculated based on all sulfur sites, the activity of the interfacial sulfur sites is much higher. The above results demonstrate that the construction of the in-plane heterostructure efficiently activated the basal planes of 1 T-MoS₂.

We further investigated the catalytic performance of TMSs@ 1 T-MoS₂ in an alkaline media (1.0 M KOH) (Fig. S12a). The catalysts follow the same order in activity as in the acidic media. Specifically, the η_{10} of 1 T-MoS₂ NSs, FeS₂ @ 1 T-MoS₂, CoS₂ @ 1 T-MoS₂, and NiS₂ @ 1 T-MoS₂ are 169, 161, 95, and 71 mV, respectively. Moreover, in comparison to the large Tafel slope of 1 T-MoS₂ NSs (82 mV dec⁻¹), FeS₂ @ 1 T-MoS₂, CoS₂ @ 1 T-MoS₂, and NiS₂ @ 1 T-MoS₂ reveal decreased Tafel slopes of 56, 45, and 40 mV dec⁻¹, respectively, implying accelerated reaction kinetics (Fig. S12b). Especially, the Tafel slope of 40 mV dec⁻¹ for the NiS₂ @ 1 T-MoS₂ indicates that the rate-determining step is the Heyrovsky step, rather than the Volmer step involving water dissociation. The chronoamperometric tests demonstrate a high electrochemical stability of TMSs@ 1 T-MoS₂ (> 30 h) in alkaline media (Fig. S13). TMSs@ 1 T-MoS₂ catalysts maintain up to 96% of the current density, better than 1 T-MoS₂ NSs with 86% current density remaining. Moreover, the SEM images (Fig. S14) and XPS results (Fig. S15) of the post-chronoamperometry catalyst show that the morphology and phase composition of TMSs@ 1 T-MoS₂ are well preserved, confirming their excellent stability. Moreover, similar to that in the acidic electrolyte, the TMSs@ 1 T-MoS₂ exhibited increased j_0 (Fig. S16a), TOF values (Fig. S16b), and increased activity in ECSA-normalized LSV (Fig. S17). Furthermore, as the EIS (Fig. S18) illustrated, the charge transfer kinetics of TMSs@ 1 T-MoS₂ are also optimized. In brief, in comparison to 1 T-MoS₂ NSs, the in-plane heterostructures exhibited significantly enhanced catalytic activity in both acidic and alkaline media, which is primarily attributed to the improvement in the intrinsic activity of the sulfur sites on the basal plane.

5. Origin of the catalytic activity of TMSs@ 1 T-MoS₂

We conducted density functional theory (DFT) calculations to reveal the mechanism of the dramatically enhanced catalytic activity of TMSs@ 1 T-MoS₂. The calculation structural models are constructed according to experimental observations in which TMSs, i.e. FeS₂, CoS₂, and NiS₂ grains, are embedded in the lattice of 1 T-MoS₂, respectively, and share S atoms at the heterointerface with 1 T-MoS₂ (Fig. S19 e-g). First, we explored the thermodynamic possibility for the formation of TMSs@ 1 T-MoS₂ based on calculating the formation energy (Fig. S20). The FeS₂ @ 1 T-MoS₂, CoS₂ @ 1 T-MoS₂, and NiS₂ @ 1 T-MoS₂ exhibit formation energies of -2.41, -2.40, and -2.36 eV, respectively, which are lower than that of pristine 1 T-MoS₂ (-2.12 eV). Since out-of-plane heterostructures where the loaded phases lie on the top of the 1 T-MoS₂ nanosheets have been extensively studied in previous works [51–54], we calculated the formation energies of TMSs/1 T-MoS₂ out-of-plane heterostructures (Fig. S19b-d) for comparison. The FeS₂/1 T-MoS₂, CoS₂/1 T-MoS₂, and NiS₂/1 T-MoS₂ out-of-plane heterostructures show higher formation energies of -1.96, -1.94, and -1.84 eV, respectively. The lower formation energy of TMSs@ 1 T-MoS₂ suggests the formation of in-plane structures is thermodynamically more favorable.

In general, when two phases combine to form a heterostructure, the lattice mismatch between the phases tends to deform the lattice at the interfaces. We measured the crystal plane spacing of the calculated structural models to examine the effect of TMSs insertion on the 1 T-MoS₂ lattice (Table S3). The calculations suggest that the (100) interplanar spacings expand by 0.115, 0.113, and 0.141 Å for the FeS₂ @ 1 T-MoS₂, CoS₂ @ 1 T-MoS₂, and NiS₂ @ 1 T-MoS₂, respectively, while the interlayer spacings, i.e., the (002) crystal plane spacings, shrink by 0.418, 0.332, and 0.312 Å, respectively, as consistent with the TEM,

XRD, and GPA results. As is well-known, the (100) crystal planes are joined by in-plane covalent bonding, while the (002) crystal planes are connected by out-of-plane van der Waals forces. As a short-range force, the covalent bonding has a stronger effect on the 1 T-MoS₂ lattice than the van der Waals forces. Hence, the expansion of the (100) interplanar spacing has a greater impact on the electron structure of 1 T-MoS₂. Additionally, the density of state (DOS) analysis supports this view, which will be discussed later. Moreover, we compared the lattice distortion of the in-plane and the out-of-plane heterostructures. The out-of-plane heterostructures, i.e., FeS₂/1 T-MoS₂, CoS₂/1 T-MoS₂, and NiS₂/1 T-MoS₂ have no discernable lattice distortions (Table S3). It indicates that in the in-plane heterostructures the lattice is strongly disturbed by the strong covalent bonds between the heterogeneous phases. By contrast, it is imperceptible in the out-of-plane heterostructures connected by weak van der Waals forces.

Generally speaking, the hydrogen absorption free energy (ΔG_H) is used to describe the intrinsic catalytic activity of HER catalysts, where an ideal activity is achieved when its value is close to 0 eV. Thus, we calculated the ΔG_H of the TMSs@ 1 T-MoS₂ and found that the bridging S sites account for the HER activity (Fig. 4a and S21). The ΔG_H values for these bridging S sites in FeS₂ @ 1 T-MoS₂, CoS₂ @ 1 T-MoS₂, and NiS₂ @ 1 T-MoS₂ are 0.26, 0.24, and 0.22 eV, respectively, which are much smaller than that of the basal S sites of pristine 1 T-MoS₂ (0.81 eV). Surprisingly, the $|\Delta G_H|$ values of these S sites are comparable to that of the edge sites in 1 T-MoS₂ (0.23 eV), which has been proven to be extremely active. The optimized ΔG_H values suggest that embedding TMSs into 1 T-MoS₂ nanosheets enhances the adsorption capacity of basal S atoms toward the hydrogen atoms, thus promoting intrinsic activity. Additionally, considering the excellent catalytic activity of TMSs@ 1 T-MoS₂ in the alkaline media, we investigated the energy for the water dissociation (Fig. S22), which is generally regarded as the dominant step in the alkaline HER process. The energy barrier for water dissociation on TMSs@ 1 T-MoS₂ is significantly lower than that on 1 T-MoS₂ NSs by 2.1, 2.5, and 2.8 eV for FeS₂ @ 1 T-MoS₂, CoS₂ @ 1 T-MoS₂, and NiS₂ @ 1 T-MoS₂, respectively (Fig. S23 and Table S4). It indicates that the construction of in-plane heterostructures accelerates the dissociation of water molecules, thus enhancing the catalytic activity towards the alkaline HER.

We further studied their electronic structures to understand the high HER catalytic activity of TMSs@ 1 T-MoS₂. Taking NiS₂ @ 1 T-MoS₂ as an example, the differential charge density (Fig. 4b) analysis shows that an obvious charge arrangement occurs at the heterointerface. The deformed charge distributes densely between the interfacial atoms, indicating that the two phases are tightly bound by covalent bonds. Specifically, electrons are accumulated near the Mo atoms and the bridging S atoms (yellow region represents an increase in electron density), while the Ni atoms exhibit electron-deficient features (cyan color represents a decrease in electron density). It suggests that the electrons transfer from NiS₂ to 1 T-MoS₂ at the heterointerface, in agreement with the XPS results. The changes in the electron density will influence the adsorption of reactants and intermediates on the active sites. In particular, the electron-rich S atoms at the heterointerface favor the adsorption of hydrogen. The other two in-plane heterostructures (FeS₂ @ 1 T-MoS₂ and CoS₂ @ 1 T-MoS₂) also exhibit similar electronic arrangements (Fig. S24). We conducted a DOS analysis to gain more information on the electronic structures. The total DOS (TDOS) of pristine 1 T-MoS₂ has no band gap and exhibits metal-like conductivity [12,13,21]. However, after the adsorption of hydrogen atoms, the resulting 1 T-MoS₂-H exhibits a band gap of 0.36 eV (Fig. S25a), indicating a transformation to a semiconductor. By contrast, FeS₂ @ 1 T-MoS₂-H, CoS₂ @ 1 T-MoS₂-H, and NiS₂ @ 1 T-MoS₂-H exhibit a continuous DOS distribution around the Fermi level (Fig. S25b-d). It implies that the in-plane heterostructures maintain superior conductivity during the HER process. Moreover, the DOS gradually increases in the order of Fe < Co < Ni. Then, we investigated the local DOS (LDOS) of Mo (Fig. 4c) to examine the contribution of transition metals, since

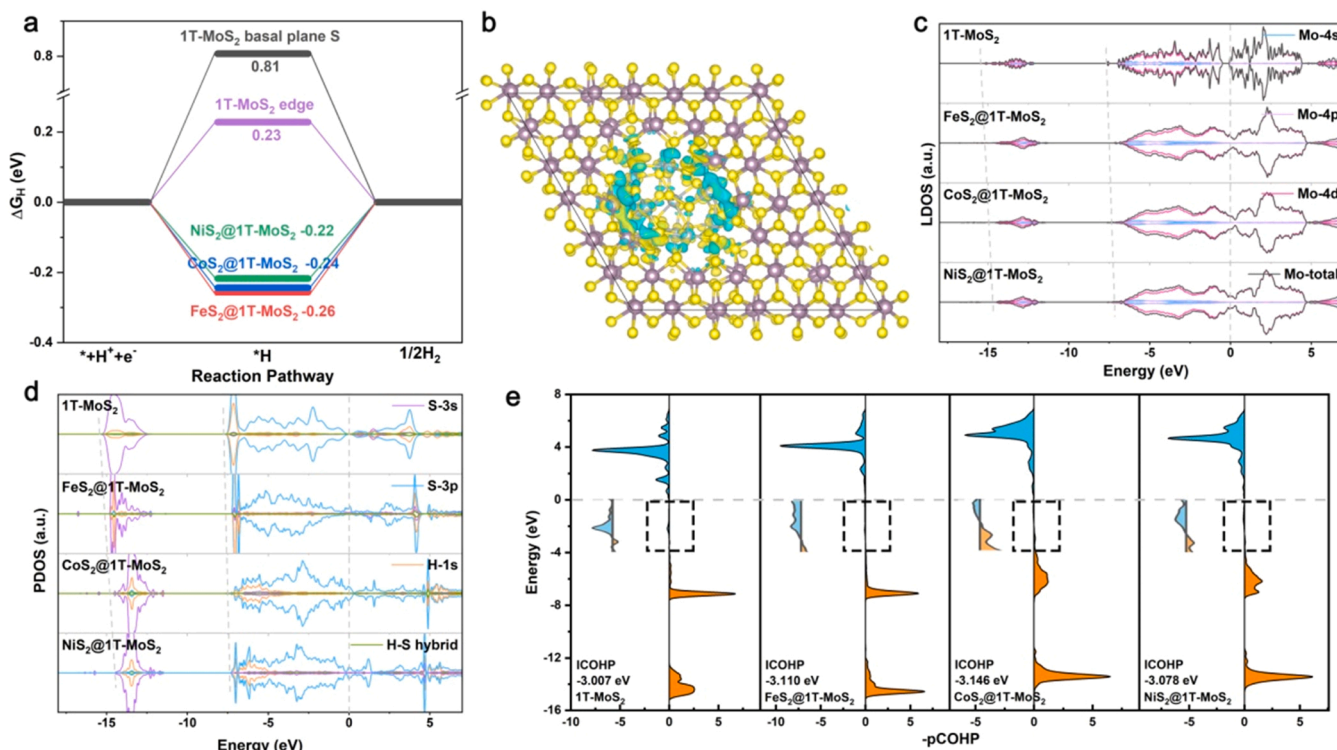


Fig. 4. a) Gibbs free energy for hydrogen adsorption of pristine 1 T-MoS₂ and the TMSs@ 1 T-MoS₂, b) Bader charge analysis of NiS₂ @ 1 T-MoS₂, c) Mo-LDOS, d) S and H-PDOS, and e) COHP of pristine 1 T-MoS₂ and the TMSs@ 1 T-MoS₂. Color code in (b): electron accumulation, yellow region; electron deficiency, cyan region, Mo, violet; S, yellow; Ni, gray.

the electronic structure of MoS₂ is mainly influenced by the coordination environment of Mo and its d-electron counts [55]. The LDOS of TMSs@ 1 T-MoS₂ reveals a contraction in electron orbitals and an upward shift towards the Fermi level in comparison to that of pristine 1 T-MoS₂. It is consistent with the previously reported strain effect arising from lattice expansion [56]. On the other hand, the d-electron counts of Fe (3d⁶ 4 s²), Co (3d⁷ 4 s²), and Ni (3d⁸ 4 s²) increase sequentially and are all larger than that of Mo (4d⁴ 4 s¹). Combined with the tendency of electron transfer as demonstrated by XPS analysis and differential charge density analysis, the electronic effect increases the efficient d-electron counts of Mo orbitals and fills the valence band top. The strain effect and electron effect synergistically maintain the metal-like conductivity during the catalytic process. Further, we employed partial DOS (PDOS) (Fig. 4d) to investigate the electronic structure variation of S atoms that are directly bonded with hydrogen atoms during the catalytic reaction. Generally, when hydrogen atoms are adsorbed on the 1 T-MoS₂, the H 1 s orbitals and S 3p orbitals undergo orbital hybridization to form fully filled bonding orbitals (H-S) with lower energy and partially filled anti-bonding orbitals (H-S)* with higher energy. The PDOS diagram of pristine 1 T-MoS₂ confirms that hydrogen adsorption induces an overlapping of H-1 s and S-3p orbitals, resulting in H-S hybridized orbitals. Similar phenomena occur for TMSs@ 1 T-MoS₂, except that the H-1 s orbitals that overlap the S-3p orbitals have a broader energy distribution than the pristine 1 T-MoS₂. It suggests that after implanting TMSs, the orbital hybridization of the adsorbed hydrogen and the S atom strengthens, which helps stabilize the H-S bond. The strain effect is particularly noticeable in the S-electron orbitals, where the S-3 s and S-3p orbitals both display certain degrees of upward shift and contraction in energy distribution. The NiS₂ @ 1 T-MoS₂, which has the greatest in-plane lattice expansion, exhibits the most dramatic upward shift and contraction in energy distribution. This upward shift can push the (H-S)* orbitals outward the Fermi level, strengthening H-S bonds. On the contrary, the electron transfer from TMSs to 1 T-MoS₂ (electron effect) results in electron filling in the (H-S)

* neighboring Fermi level, thus weakening H-S bonding. To verify the bonding stability of H-S, we conducted a crystal orbital Hamiltonian population quantization (COHP) study. (Fig. 4e). The pristine 1 T-MoS₂ displays (H-S) orbitals below the Fermi level as well as (H-S)* orbitals across the Fermi level, with an ICOHP value of -3.007 eV. After embedding TMSs, the (H-S)* content under the Fermi level decreases. Moreover, the ICOHP values of FeS₂ @ 1 T-MoS₂, CoS₂ @ 1 T-MoS₂, and NiS₂ @ 1 T-MoS₂ are -3.110, -3.1145, and -3.078 eV, respectively. The lower ICOHP values of TMSs@ 1 T-MoS₂ correspond to more stable H-S bonds and consequently enhanced hydrogen adsorption capacity. These results suggest that the lattice expansion-induced decrease in (H-S)* orbital content dominates in regulating the electronic structure.

Briefly, we found that the embedding of TMSs induces the expansion of the 1 T-MoS₂ lattice and the electron transfer at the interface. Both effects, i.e. the strain effect and the electron effect, regulate the electronic structure and work synergistically to endow the TMSs@ 1 T-MoS₂ with outstanding conductivity and improved hydrogen adsorption capacity. Consequently, the catalytic activity of the TMSs@ 1 T-MoS₂ in-plane heterostructure is significantly enhanced.

6. Conclusion

In summary, we constructed TMSs@ 1 T-MoS₂ in-plane heterostructures where the TMSs clusters substitute a portion of 1 T-MoS₂ nanodomains and embed in the 1 T-MoS₂ nanosheets. Both experimental and DFT results indicate that this unique structure induces an electron transfer from TMSs to 1 T-MoS₂, as well as an expansion in the in-plane lattice and a contraction in interlayer spacing in 1 T-MoS₂. These changes lead to an electron effect and a strain effect that synergistically modulate the electronic structure of the bridging S atoms, thus significantly boosting the catalytic activity. Besides, this unique structure enables full exposure of active sites. Benefiting from these advantages, TMSs@ 1 T-MoS₂, especially NiS₂ @ 1 T-MoS₂, outperformed excellent HER activity by delivering a current density of 10 mA cm⁻² at

lower overpotentials of 73 and 71 mV in acidic and alkaline electrolytes, respectively. This work may provide new insight into designing advanced two-dimensional layered material electrocatalysts.

CRedit authorship contribution statement

Kaiwen Wang: Data curation, Writing – original draft preparation. **Kaifeng Yu:** Project administration. **Shaonan Xu:** Project administration. **Shisheng Yuan:** Data curation. **Lijuan Xiang:** Visualization. **Bingxue Pang:** Investigation. **Jiaqi Zheng:** Investigation. **Nan Li:** Writing – review & editing, Funding acquisition.

Declaration of Competing Interest

The authors declare that they have no known competing financial interests or personal relationships that could have appeared to influence the work reported in this paper.

Data Availability

Data will be made available on request.

Acknowledgments

This study was supported by the National Natural Science Foundation of China (22072056).

Appendix A. Supporting information

Supplementary data associated with this article can be found in the online version at [doi:10.1016/j.apcatb.2023.122445](https://doi.org/10.1016/j.apcatb.2023.122445).

References

- [1] Z. He, W. Que, Molybdenum disulfide nanomaterials: structures, properties, synthesis and recent progress on hydrogen evolution reaction, *Appl. Mater. Today* 3 (2016) 23–56.
- [2] M. Chhowalla, H.S. Shin, G. Eda, L.-J. Li, K.P. Loh, H. Zhang, The chemistry of two-dimensional layered transition metal dichalcogenide nanosheets, *Nat. Chem.* 5 (2013) 263–275.
- [3] S. Ali Shah, R. Sayyar, L. Xu, H. Sun, I. Khan, J. Guo, X. Shen, S. Hussain, A. Yuan, H. Ullah, In-situ synthesis of NiS₂ nanoparticles/MoS₂ nanosheets hierarchical sphere anchored on reduced graphene oxide for enhanced electrocatalytic hydrogen evolution reaction, *J. Colloid Interf. Sci.* 624 (2022) 150–159.
- [4] S. Ali Shah, L. Xu, R. Sayyar, T. Bian, Z. Liu, A. Yuan, X. Shen, I. Khan, A. Ali Tahir, H. Ullah, Growth of MoS₂ nanosheets on M@N-doped carbon particles (M = Co, Fe or CoFe Alloy) as an efficient electrocatalyst toward hydrogen evolution reaction, *Chem. Eng. J.* 428 (2022), 132126.
- [5] M.T.T. Zhenbin Wang, Ang Cao, Karen Chan, K. Jens, Nørskov, Insights into the hydrogen evolution reaction on 2D transition metal dichalcogenides, *J. Phys. Chem. C* 126 (2022) 5151–5158.
- [6] X. Chia, M. Pumera, Characteristics and performance of two-dimensional materials for electrocatalysis, *Nat. Catal.* 1 (2018) 909–921.
- [7] Y. Xu, R. Ge, J. Yang, J. Li, S. Li, Y. Li, J. Zhang, J. Feng, B. Liu, W. Li, Molybdenum disulfide (MoS₂)-based electrocatalysts for hydrogen evolution reaction—from mechanism to manipulation, *J. Energy Chem.* 74 (2022) 45–71.
- [8] Y. Gao, S. Wang, B. Wang, Z. Jiang, T. Fang, Recent progress in phase regulation, functionalization, and biosensing applications of polyphase MoS₂, *Small* 18 (2022), e2202956.
- [9] J.W. Lina Liu, Liyuan Wu, Meng Ye, Xiaozhi Liu, Qian Wang, Siyao Hou, Pengfei Lu, Lifei Sun, Jingying Zheng, Lei Xing, Lin Gu, Xiangwei Jiang, Liming Xie, Liying Jiao, Phase-selective synthesis of 1T'-MoS₂ monolayers and heterophase bilayers, *Nat. Mater.* 17 (2017) 1108–1114.
- [10] M. Humayun, H. Ullah, Z.-E. Cheng, A.A. Tahir, W. Luo, C. Wang, Au surface plasmon resonance promoted charge transfer in Z-scheme system enables exceptional photocatalytic hydrogen evolution, *Appl. Catal. B-Environ.* 310 (2022), 121322.
- [11] B. Seo, S.H. Joo, Recent advances in unveiling active sites in molybdenum sulfide-based electrocatalysts for the hydrogen evolution reaction, *Nano Conver.* 4 (2017) 19–30.
- [12] Z. Sadighi, J. Liu, L. Zhao, F. Ciucci, J.-K. Kim, Metallic MoS₂ nanosheets: multifunctional electrocatalyst for the ORR, OER and Li-O₂ batteries, *Nanoscale* 10 (2018) 22549–22559.
- [13] Y. Jiao, A.M. Hafez, D. Cao, A. Mukhopadhyay, Y. Ma, H. Zhu, Metallic MoS₂ for high performance energy storage and energy conversion, *Small* 14 (2018), e1800640.
- [14] D. Voiry, M. Salehi, R. Silva, T. Fujita, M. Chen, T. Asefa, V.B. Shenoy, G. Eda, M. Chhowalla, Conducting MoS₂ nanosheets as catalysts for hydrogen evolution reaction, *Nano. Lett.* 13 (2013) 6222–6227.
- [15] M. Liu, C. Zhang, A. Han, L. Wang, Y. Sun, C. Zhu, R. Li, S. Ye, Modulation of morphology and electronic structure on MoS₂-based electrocatalysts for water splitting, *Nano Res.* 15 (2022) 6862–6887.
- [16] S. Niu, J. Cai, G. Wang, Two-dimensional MoS₂ for hydrogen evolution reaction catalysis: the electronic structure regulation, *Nano Res.* 14 (2020) 1985–2022.
- [17] S. Sovizi, R. Szożkiewicz, Single atom doping in 2D layered MoS₂ from a periodic table perspective, *Surf. Sci. Rep.* 77 (2022).
- [18] M.C. Hui Li, Peng Wang, Ruofan Du, Luying Song, Jun He, Jianping Shi, Reducing contact resistance and boosting device performance of monolayer MoS₂ by in-situ Fe doping, *Adv. Mater.* 34 (2022) 2200885.
- [19] L. Li, Z. Qin, L. Ries, S. Hong, T. Michel, J. Yang, C. Salameh, M. Bechelany, P. Miele, D. Kaplan, M. Chhowalla, D. Voiry, Role of sulfur vacancies and undercoordinated Mo regions in MoS₂ nanosheets toward the evolution of hydrogen, *ACS Nano* 13 (2019) 6824–6834.
- [20] S. Jayabal, G. Saranya, J. Wu, Y. Liu, D. Geng, X. Meng, Understanding the high-electrocatalytic performance of two-dimensional MoS₂ nanosheets and their composite materials, *J. Mater. Chem. A* 5 (2017) 24540–24563.
- [21] Y. Lv, P. Chen, J.J. Foo, J. Zhang, W. Qian, C. Chen, W.J. Ong, Dimensionality-dependent MoS₂ toward efficient photocatalytic hydrogen evolution: from synthesis to modifications in doping, surface and heterojunction engineering, *Mater. Today Nano* 18 (2022), 100191.
- [22] Y. Cao, Roadmap and direction toward high-performance MoS₂ hydrogen evolution catalysts, *ACS Nano* (2021) 11014–11039.
- [23] O. Samy, A. El Moutaouakil, A review on MoS₂ energy applications: recent developments and challenges, *Energies* 14 (2021) 4586.
- [24] U. Krishnan, M. Kaur, K. Singh, M. Kumar, A. Kumar, A synoptic review of MoS₂: synthesis to applications, *Superlattice. Microstruct.* 128 (2019) 274–297.
- [25] Y. Feng, T. Zhang, J. Zhang, H. Fan, C. He, J. Song, 3D 1T-MoS₂/CoS₂ heterostructure via interface engineering for ultrafast hydrogen evolution reaction, *Small* (2020), e2002850.
- [26] Y. Yang, H. Yao, Z. Yu, S.M. Islam, H. He, M. Yuan, Y. Yue, K. Xu, W. Hao, G. Sun, H. Li, S. Ma, P. Zapol, M.G. Kanatzidis, Hierarchical nanoassembly of MoS₂/Co₉S₈/Ni₃S₂/Ni as a highly efficient electrocatalyst for overall water splitting in a wide pH range, *J. Am. Chem. Soc.* 141 (2019) 10417–10430.
- [27] Z. Liu, K. Wang, Y. Li, S. Yuan, G. Huang, X. Li, N. Li, Activation engineering on metallic 1T-MoS₂ by constructing in-plane heterostructure for efficient hydrogen generation, *Appl. Catal. B-Environ.* 300 (2022) 120696–120703.
- [28] C.W. Nan Zhang, Feng Zhao, Kuo Han, Yejin Ma, Yue Li, Jian Liu, Self-healing γ-FeOOH decorated onto MoS₂ nanosheets for boosting the hydrogen evolution in alkaline media, *Appl. Catal. B-Environ.* 297 (2021) 120456–120465.
- [29] M. Kim, M.A.R. Anjum, M. Choi, H.Y. Jeong, S.H. Choi, N. Park, J.S. Lee, Covalent 0D–2D heterostructuring of Co₉S₈–MoS₂ for enhanced hydrogen evolution in all pH electrolytes, *Adv. Funct. Mater.* 30 (2020) 2002536–2002546.
- [30] C. Zhao, R. Wang, Y. Zhang, L. Chen, T. Li, X. Deng, P. Zhang, X. Lu, Electrostatic force-driven anchoring of Ni(OH)₂ nanocrystallites on single-layer MoS₂ for high-performance asymmetric hybrid supercapacitors, *Electrochim. Acta* 320 (2019), 134591.
- [31] L. Xu, S. Ali Shah, H. Khan, R. Sayyar, X. Shen, I. Khan, A. Yuan, W. Yaseen, Z. Ali Ghazi, A. Naem, H. Ullah, X. Li, C. Wang, Ni₃S₂ nanostrips@FeNi-NiFe₂O₄ nanoparticles embedded in N-doped carbon microsphere: an improved electrocatalyst for oxygen evolution reaction, *J. Colloid Interf. Sci.* 617 (2022) 1–10.
- [32] Q. Tang, D.-e. Jiang, Mechanism of hydrogen evolution reaction on 1T-MoS₂ from first principles, *ACS Catal.* 6 (2016) 4953–4961.
- [33] Z. Zhu, H. Yin, C.-T. He, M. Al-Mamun, P. Liu, L. Jiang, Y. Zhao, Y. Wang, H.-G. Yang, Z. Tang, D. Wang, X.-M. Chen, H. Zhao, Ultrathin transition metal dichalcogenide/3d metal hydroxide hybridized nanosheets to enhance hydrogen evolution activity, *Adv. Mater.* 30 (2018) 1801171–1801177.
- [34] G. Kresse, Efficient iterative schemes for ab initio total-energy calculations using a plane-wave basis set, *Phys. Rev. B* 54 (1996) 11169–11186.
- [35] P.E. Blochl, Projector augmented-wave method, *Phys. Rev. B Condens. Matter* 50 (1994) 17953–17979.
- [36] K.B. John, P. Perdew, M. Ernzerhof, Generalized Gradient Approximation Made Simple, *Phys. Rev. Lett.* 77 (1996) 3865–3868.
- [37] S.A. Shah, L. Xu, R. Sayyar, I. Khan, A. Yuan, X. Shen, X. Li, H. Ullah, FeNi@N-doped graphene core-shell nanoparticles on carbon matrix coupled with MoS₂ nanosheets as a competent electrocatalyst for efficient hydrogen evolution reaction, *Adv. Mater. Interfaces* 9 (2022) 2201040.
- [38] Y.X. Zhihua Cheng, Wenpeng Wu, Xinqun Zhang, Qiang Fu, Yang Zhao, Liangti Qu, All-pH-tolerant in-plane heterostructures for efficient hydrogen evolution reaction, *ACS Nano* 15 (2021) 11417–11427.
- [39] P. Chang, T. Wang, Z. Liu, X. Wang, J. Zhang, H. Xiao, L. Guan, J. Tao, Interface-assisted phase transition in MOF-derived MoS₂/CoS₂ heterostructures for highly efficient dual-pH hydrogen evolution and overall water splitting, *J. Mater. Chem. A* 10 (2022) 16115–16126.
- [40] X. Li, X. Lv, X. Sun, C. Yang, Y.-Z. Zheng, L. Yang, S. Li, X. Tao, Edge-oriented, high-percentage 1T'-phase MoS₂ nanosheets stabilize Ti₃C₂ MXene for efficient electrocatalytic hydrogen evolution, *Appl. Catal. B-Environ.* 284 (2021), 119708.
- [41] S.Y. Zhiqiang Xie, Xiaohan Ma, Kui Li, Lei Ding, Weitian Wang, David A. Cullen, Harry M. Meyer III, Haoran Yu, Jianhua Tong, Zili Wu, Feng-Yuan Zhang, MoS₂ nanosheet integrated electrodes with engineered ¹T–²H phases and defects for efficient hydrogen production in practical PEM electrolysis, *Appl. Catal. B-Environ.* 313 (2022), 121458.

- [42] Z. Li, X. Yan, D. He, W. Hu, S. Younan, Z. Ke, M. Patrick, X. Xiao, J. Huang, H. Wu, X. Pan, J. Gu, Manipulating coordination structures of mixed-valence copper single atoms on 1T-MoS₂ for efficient hydrogen evolution, *ACS Catal.* 12 (2022) 7687–7695.
- [43] T. Zhang, T. Yang, G. Qu, S. Huang, P. Cao, W. Gao, Phase control and stabilization of 1T-MoS₂ via black TiO₂-nanotube arrays supporting for electrocatalytic hydrogen evolution, *J. Energy Chem.* 68 (2022) 71–77.
- [44] G. Wang, G. Zhang, X. Ke, X. Chen, X. Chen, Y. Wang, G. Huang, J. Dong, S. Chu, M. Sui, Direct synthesis of stable 1T-MoS₂ doped with Ni single atoms for water splitting in alkaline media, *Small* 18 (2022), e2107238.
- [45] Y. Huang, Y. Sun, X. Zheng, T. Aoki, B. Pattengale, J. Huang, X. He, W. Bian, S. Younan, N. Williams, J. Hu, J. Ge, N. Pu, X. Yan, X. Pan, L. Zhang, Y. Wei, J. Gu, Atomically engineering activation sites onto metallic 1T-MoS₂ catalysts for enhanced electrochemical hydrogen evolution, *Nat. Commun.* 10 (2019) 982–992.
- [46] C.C. Gudal, U.N. Pan, D.R. Paudel, M.R. Kandel, N.H. Kim, J.H. Lee, Bifunctional P-intercalated and doped metallic (1T)-copper molybdenum sulfide ultrathin 2D-nanosheets with enlarged interlayers for efficient overall water splitting, *ACS Appl. Mater. Inter.* 14 (2022) 14492–14503.
- [47] Y. Chen, G. Meng, T. Yang, C. Chen, Z. Chang, F. Kong, H. Tian, X. Cui, X. Hou, J. Shi, Interfacial engineering of Co-doped 1T-MoS₂ coupled with V₂C MXene for efficient electrocatalytic hydrogen evolution, *Chem. Eng. J.* 450 (2022), 138157.
- [48] B. Gao, Y. Zhao, X. Du, Y. Chen, B. Guan, Y. Li, Y. Li, S. Ding, H. Zhao, C. Xiao, Z. Song, Facile phase transition engineering of MoS₂ for electrochemical hydrogen evolution, *J. Mater. Chem. A* 9 (2021) 8394–8400.
- [49] Z. Liu, L. Zhao, Y. Liu, Z. Gao, S. Yuan, X. Li, N. Li, S. Miao, Vertical nanosheet array of 1T phase MoS₂ for efficient and stable hydrogen evolution, *Appl. Catal. B-Environ.* 246 (2019) 296–302.
- [50] Z. Liu, Z. Gao, Y. Liu, M. Xia, R. Wang, N. Li, Heterogeneous nanostructure based on 1T-Phase MoS₂ for enhanced electrocatalytic hydrogen evolution, *ACS Appl. Mater. Inter.* 9 (2017) 25291–25297.
- [51] Z.L. Kaiwen Wang, Qian Gao, Nan Li, Kaifeng Yu, Ni(OH)₂ nanoparticles decorated on 1T phase MoS₂ basal plane for efficient water splitting, *Appl. Surf. Sci.* 593 (2022), 153408.
- [52] G. Zhou, X. Wu, M. Zhao, H. Pang, L. Xu, J. Yang, Y. Tang, Interfacial engineering-triggered bifunctionality of CoS₂/MoS₂ nanocubes/nanosheet arrays for high-efficiency overall water splitting, *ChemSusChem* 14 (2021) 699–708.
- [53] M. Liu, J.A. Wang, W. Klysubun, G.G. Wang, S. Sattayaporn, F. Li, Y.W. Cai, F. Zhang, J. Yu, Y. Yang, Interfacial electronic structure engineering on molybdenum sulfide for robust dual-pH hydrogen evolution, *Nat. Commun.* 12 (2021) 5260.
- [54] K. Wang, S. Xu, K. Yu, Z. Liu, S. Yuan, L. Xiang, Y. Zhang, N. Li, Heterostructure induced S p-band center shift for activating 1T-MoS₂ basal plane towards hydrogen evolution reaction, *ChemNanoMat* 8 (2022) 202200328.
- [55] M.A. Lukowski, A.S. Daniel, F. Meng, A. Forticaux, L. Li, S. Jin, Enhanced hydrogen evolution catalysis from chemically exfoliated metallic MoS₂ nanosheets, *J. Am. Chem. Soc.* 135 (2013) 10274–10277.
- [56] X.Za.X.Z. Xuan Ai, Transition-Metal-Boron Intermetallics with Strong Interatomic d-sp Orbital Hybridization for High-Performance Electrocatalysis, *Angew. Chem. Int. Ed* (2020) 3961–3965.